



HOKKAIDO UNIVERSITY

Title	Extinction law in ultraluminous infrared galaxies at $z \sim 1$
Author(s)	Shimizu, T.; Kawara, K.; Sameshima, H. et al.
Citation	Monthly Notices of the Royal Astronomical Society, 418(1), 625-637 https://doi.org/10.1111/j.1365-2966.2011.19512.x
Issue Date	2011-11
Doc URL	https://hdl.handle.net/2115/49111
Type	journal article
File Information	MNRAS418-1_625-637.pdf



Extinction law in ultraluminous infrared galaxies at $z \sim 1$

T. Shimizu,¹* K. Kawara,¹* H. Sameshima,¹ N. Ienaka,¹ T. Nozawa² and T. Kozasa³

¹*Institute of Astronomy, The University of Tokyo, Osawa 2-21-1, Mitaka, Tokyo 181-0015, Japan*

²*Institute for the Physics and Mathematics of the Universe, The University of Tokyo, 5-1-5 Kashiwanoha, Kashiwa 277-8568, Japan*

³*Department of CosmoSciences, Hokkaido University, Sapporo 060-0810, Japan*

Accepted 2011 July 26. Received 2011 July 26; in original form 2011 May 5

ABSTRACT

We analyse the multiwavelength photometric and spectroscopic data of 12 ultraluminous infrared galaxies (ULIRGs) at $z \sim 1$ and compare them with models of stars and dust in order to study the extinction law and star formation in young infrared (IR) galaxies. Five extinction curves, namely the Milky Way (MW), the pseudo-MW which is MW-like without the 2175 Å feature, the Calzetti and two supernova (SN) dust curves are applied to the data by combining with various dust distributions, namely the uniform dust screen, the clumpy dust screen, the internal dust geometry, and the composite geometry with a combination of dust screen and internal dust. Employing a minimum χ^2 method, we find that the foreground dust screen geometry, especially combined with the 8–40 M_{\odot} SN extinction curve, provides a good approximation to the real dust geometry, whereas internal dust is only significant in two galaxies. The SN extinction curves, which are flatter than the others, reproduce the data of eight (67 per cent) galaxies better. Dust masses are estimated to be in excess of $\sim 10^8 M_{\odot}$. The inferred ages of the galaxies are small, eight of which range from 10 to 650 Myr. The SN-origin dust is the most plausible to account for the vast amount of dust masses and the flat slope of the observed extinction law. The inferred dust mass per SN ranges from 0.01 to 0.4 M_{\odot} per SN.

Key words: supernovae: general – dust, extinction – galaxies: evolution – galaxies: ISM – galaxies: starburst – infrared: galaxies.

1 INTRODUCTION

Recent developments in far-infrared (FIR) and submillimetre astronomy have revealed new populations of galaxies associated with thermal dust emission, such as dusty quasars and infrared galaxies. Thermal dust emission detected in quasars and galaxies at high redshifts exhibits inferred dust mass in excess of $\sim 10^8 M_{\odot}$. Such a vast amount of dust observed at $z \gtrsim 6$ (Bertoldi et al. 2003; Robson et al. 2004; Beelen et al. 2006) strongly suggests that the dust has been condensed in the ejecta of core-collapsed supernovae (SNe II) promptly after the onset of the initial star formation. Asymptotic giant branch (AGB) stars are known to be the major source of dust in the present-day Universe. However, the importance of AGB stars at high redshifts is in controversy, because they inject dust grains into the interstellar medium (ISM) only after their progenitor stars have evolved off the main sequence. While a delay time of $\gtrsim 500$ Myr since their formation has been suggested (e.g. Dwek 1998), Valiante et al. (2009) proposed that AGB stars can dominate dust production in a delay time of $\gtrsim 150$ Myr if the starburst is instantaneous.

Michałowski et al. (2010) pointed out that AGB stars are not efficient enough to form dust in dusty quasars at $z > 5$, whereas SNe II may be able to account for the dust, and underlined the importance of dust grain growth in the ISM.

Quasars have been frequently used to study the extinction law at high redshifts. This is because of their simple dust geometry, in which the central point-like emitting source is surrounded by dust grains which are physically separated from the source itself. This is analogous to the classical configuration assumed when dereddening single stars. There is a line of evidence that active galactic nuclei (AGNs) have extinction curves that differ from those observed in the Milky Way (MW) and Large and Small Magellanic Clouds (LMC and SMC). Gaskell et al. (2004) analysed a large sample of AGNs and found indications of a very flat extinction curve in ultraviolet (UV). On the other hand, exploring large samples of quasars from the Sloan Digital Sky Survey (SDSS), Richards et al. (2003) and Hopkins et al. (2004) found that the extinction law in quasars at $z < 2.2$ is described by SMC reddening but neither by LMC and SMC reddening nor by that found in the Gaskell et al. (2004) sample. Recently, Gallerani et al. (2010) proposed that quasars at $z = 3.9$ – 6.4 have reddening that deviates from that of the SMC with a tendency to flatten at $\lambda \lesssim 2000$ Å. Maiolino et al. (2004) found that SDSS J1048+4647, a broad absorption line quasar (BALQSO) at $z = 6.2$,

*E-mail: tshimizu@ioa.s.u-tokyo.ac.jp (TS); kkawara@ioa.s.u-tokyo.ac.jp (KK)

requires a flat extinction curve which is quite different from those observed in the MW, LMC and SMC, but in excellent agreement with SN extinction curves by Todini & Ferrara (2001).

Although it is reasonable to expect that the extinction law in young galaxies would be dominated by SN-condensed dust, the complications introduced by dust geometries have hampered this line of studies; the attenuation of extended starlight by dust depends not only on the optical properties of dust but also on the distribution geometry of the dust. Calzetti (2001) derived the empirical extinction law in local starbursts and blue compact galaxies, assuming that the dust geometry is described in a foreground screen, i.e. an apparent attenuation of starlight to be $e^{-\tau_\nu}$. If a dust geometry in their galaxies is indeed a foreground screen, the slope (i.e. wavelength dependence) of the extinction curve (i.e. the optical depth τ_ν) is significantly flatter than those observed in the MW, LMC and SMC. The spectral energy distribution (SED) and spectroscopic data of a young, ultraluminous infrared galaxy (ULIRG)¹ at $z \sim 1$ were analysed by Kawara et al. (2011), who found that the data require a flat extinction curve and the dust geometry of a foreground dust screen, which would result in a better agreement with the extinction curve synthesized from SN-condensed dust by Hirashita et al. (2005) than those observed in local starbursts, MW, LMC and SMC.

The slope of the extinction curve is expected to reflect the sites of dust formation and the subsequent processing in the ISM. The extinction curves can be ordered as the SMC, LMC, MW and Calzetti curves from the steepest to the flattest. The synthetic extinction curves of newly condensed dust grains in SN ejecta before the ISM reprocessing (hereafter called original SN extinction curves) are flatter than the Calzetti curve (Todini & Ferrara 2001; Nozawa et al. 2003; Maiolino et al. 2004; Hirashita et al. 2005; see also fig. 3 in Kawara et al. 2011). Then, the bulk of dust grains condensed in the ejecta is destroyed through the passage of the reverse shock (Bianchi & Schneider 2007; Nozawa et al. 2007; Hirashita et al. 2008). Finally, grains that survive the reverse shock are shattered in the warm ionized ISM (Hirashita et al. 2010). None the less, the final SN extinction curves, after taking into account the reverse shock and shattering, are expected to have a slope as flat as those of the original extinction curves. The shattering may also be important in old galaxies such as MW, LMC and SMC, where AGB stars are dominant sources of dust production, because some observations (Groenewegen 1997; Gauger et al. 1999) suggest AGB stars form large grains. Dust grain growth in the ISM would be efficient in infrared galaxies where there must be many molecular clouds near SN remnants, and it is suggested that the dust mass in the high-redshift quasars is dominated by grain growth in the ISM (Dwek 1998; Draine 2009; Michałowski et al. 2010; Valiante et al. 2011). It seems that this process results in flat extinction curves in the sense that the larger grains show the flatter extinction curve. However, the extinction laws found in the high-redshift quasars and local starbursts are flatter than those found in the MW for which Draine (2009) attributes the bulk of the dust mass to the growth of grains in the ISM.

As discussed so far, $z < 2.2$ quasars show a striking contrast in the slopes of the extinction curves against the $z \sim 1$ ULIRG and higher

redshift quasars. In this paper, we explore this issue by expanding our previous work on a single young ULIRG (Kawara et al. 2011) to 12 young ULIRGs at $z \sim 1$.

2 DATA

The sample consists of 12 infrared galaxies at $z = 0.85$ – 1.44 . The redshifts and data sources of our 12 galaxies are shown in Table 1. They are SST J1604+4304, HR10 (ERO J164502+4626.4), and 10 galaxies found in the Cosmological Evolution Survey (COSMOS) field. We have searched archives and the literature for those galaxies which meet the following criteria: (1) the FIR emission is detected; (2) the optical spectrum indicates a redshift of ~ 1 , and gaseous emission lines such as [O II] λ 3727 and/or stellar absorption lines such as Ca H/K and H I absorption lines were detected; (3) broadband photometry has been done from the UV to mid-infrared; (4) there is no contamination from foreground galaxies; (5) the bolometric luminosity is dominated by the undergoing star formation with the criterion of $f_\nu(8 \mu\text{m})/f_\nu(4.5 \mu\text{m}) < 1.9$ (Pope et al. 2008) and no obvious evidence of emission caused by an AGN such as X-ray emission. As a result, we have found these 12 galaxies all of which are classified as starburst-dominated ULIRGs.

The data for SST J1604+4304 were taken from Kawara et al. (2010) where the multiwavelength data covering the X-ray, UV/optical, infrared and radio and the optical spectrum are given. For HR10, Stern et al. (2006) compiled the multiwavelength data from the UV/optical to radio, and the optical spectrum (strictly speaking, from 2750 to 3850 Å) is given in Dey et al. (1999).

The photometric and spectroscopic data for the 10 COSMOS galaxies are available in the COSMOS archive at <http://irsa.ipac.caltech.edu/data/COSMOS/>. Fig. 1 illustrates postage stamp images of the COSMOS galaxies from u^* to 70 μm . For full details of the observations of the COSMOS galaxies, we refer the reader to Capak et al. (2007) for optical to near-infrared imaging performed on the *Hubble Space Telescope* and ground-based telescopes including the Subaru 8.3-m telescope, the Kitt Peak National Observatory (KPNO) 4-m telescope, the Cerro Tololo Inter-American Observatory (CTIO) 4-m telescope, and the Canada–France–Hawaii (CFH) 3.6-m telescope; to Sanders et al. (2007) for the COSMOS *Spitzer*

Table 1. Sample galaxies at $z \sim 1$.

No.	Name	Redshift	Reference
1	COSMOS J100121.29+023535.8	0.850	1
2	COSMOS J100125.12+024506.5	0.980	1
3	COSMOS J100158.31+023505.2	1.021	1
4	COSMOS J100143.83+015325.0	1.066	1
5	COSMOS J100021.79+014916.1	0.995	1
6	COSMOS J100030.12+020513.3	0.894	1
7	COSMOS J100123.22+021013.3	0.850	1
8	COSMOS J100100.22+021503.6	0.893	1
9	COSMOS J100008.36+022244.6	1.093	1
10	COSMOS J095910.21+022523.3	1.026	1
11	SST J1604+4304	1.135	2
12	HR10 (ERO J164502+4626.4)	1.44	3, 4

References: 1, Cosmos archive at <http://irsa.ipac.caltech.edu/>; 2, Kawara et al. (2010); 3, Stern et al. (2006); 4, Dey et al. (1999). COSMOS Photometry Catalog 2006 January; S-COSMOS IRAC four-channel Photometry Catalog 2007 June; S-COSMOS MIPS 24 μm Photometry Catalog 2008 October; S-COSMOS MIPS 70 μm Photometry Catalog v3 2009 January; COSMOS MAGELLAN Data Version 3.1 (spectroscopy); zCOSMOS data released in 2008 October (spectroscopy).

¹ Infrared galaxies are classified according to bolometric infrared luminosity $L_{\text{IR}}(8\text{--}1000 \mu\text{m})$; $L_{\text{IR}} > 10^{11} L_\odot$ as luminous infrared galaxies (LIRGs), $L_{\text{IR}} > 10^{12} L_\odot$ as ultraluminous infrared galaxies (ULIRGs), and $L_{\text{IR}} > 10^{13} L_\odot$ as hyperluminous infrared galaxies (HyLIRGs) (Sanders & Mirabel 1996).

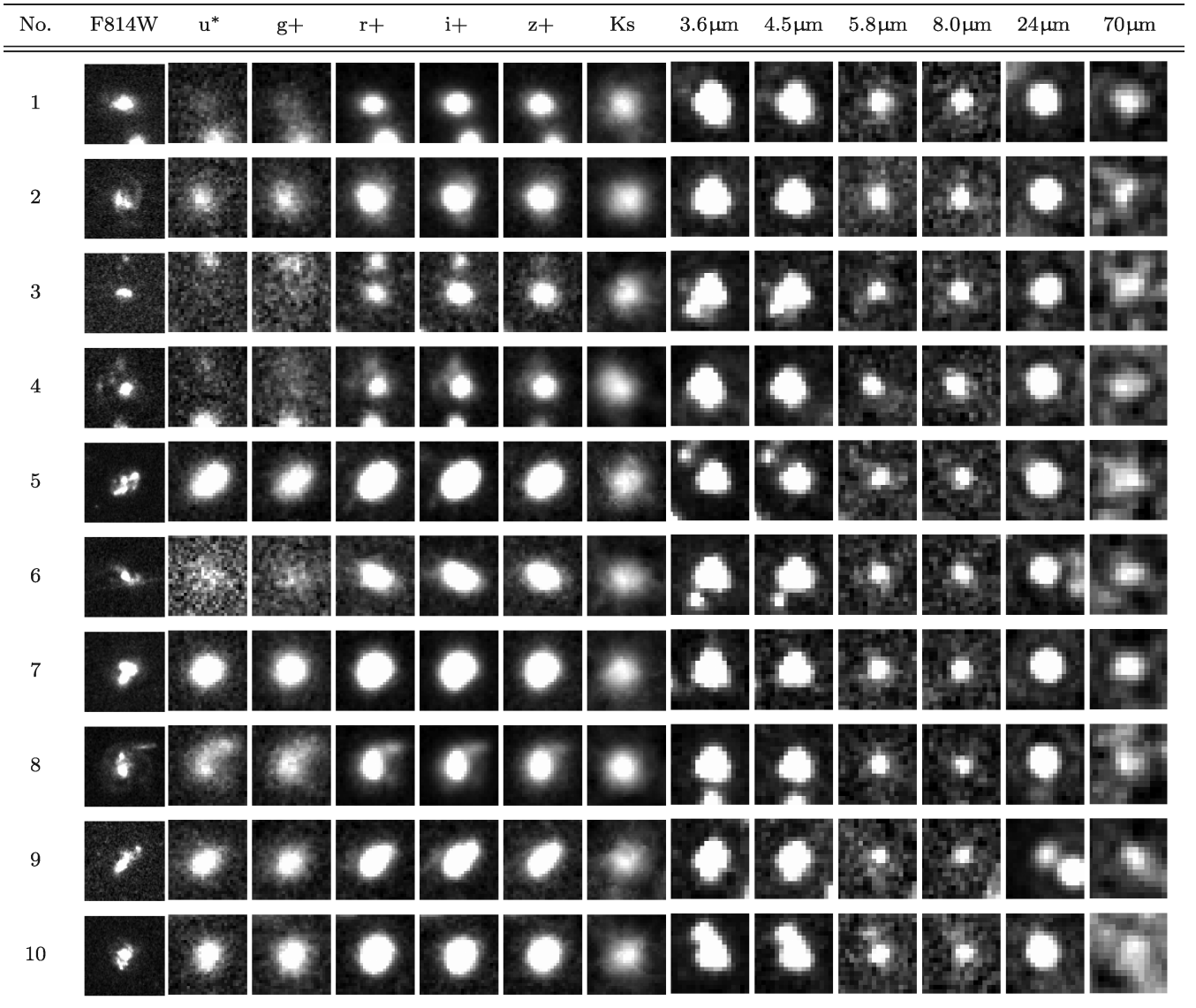


Figure 1. Postage stamp images of the 10 COSMOS galaxies. The size of each image is $4 \times 4 \text{ arcsec}^2$ for F814W to Ks, $10 \times 10 \text{ arcsec}^2$ for 3.6–8.0 μm , $20 \times 20 \text{ arcsec}^2$ for 24 μm , and $50 \times 50 \text{ arcsec}^2$ for 70 μm . North is up and east is to the left. Refer to Kawara et al. (2010) and Stern et al. (2006) for the images of No. 11 (SST J1604+4304) and No. 12 (HR10), respectively.

survey (S-COSMOS); to Le Flocc’h et al. (2009) for the 24- μm observations; to Frayer et al. (2009) for the 70- and 160- μm observations; to Trump et al. (2009) for 5600–9200 \AA spectroscopy on the Magellan 6.5-m telescope; and to Lilly et al. (2007) for 5500–9700 \AA spectroscopy on the European Southern Observatory (ESO) 8-m Very Large Telescope (VLT).

For the COSMOS galaxies, the optical counterparts of FIR sources were selected as follows. We first selected objects at $z = 0.8\text{--}1.21$ in the spectroscopy catalogues and searched for the counterparts in the optical imaging data catalogues. If there is a single object in the optical imaging data within an error circle radius of 0.2 arcsec from the spectroscopic position, we identified the spectroscopic object with the object in the optical imaging catalogues. We then searched for the mid-infrared counterpart in the IRAC (3.6, 4.5, 5.6, 8.0 μm) catalogue. Again, if there is one IRAC object within an error circle radius of 0.5 arcsec from the position of the optical, spectroscopic object, we regard the IRAC object as optically identified. This process was repeated for the 24- μm counterpart within

an error radius of 1.0 arcsec, and for the 70- μm counterpart within 4.0 arcsec. We found no 160- μm counterparts within 8.0 arcsec. As a result, we found 10 starburst-dominated ULIRGs at $z = 0.8\text{--}1.2$. Kartaltepe et al. (2010), applying more relaxed criteria than ours, found 50 70- μm sources having spectroscopic data in the same field and the same redshift range. Assuming that 70- μm sources with $>10 \text{ mJy}$ are ULIRGs at $z > 0.8$, 25 of the 50 sources are ULIRGs with spectroscopic data. They suggest that an AGN fraction is about 50 per cent, thus starburst-dominated ULIRGs are about 12, fairly consistent with the number of ULIRGs in our sample.

Optical data were taken in many photometric bands for COSMOS galaxies. If we use all these data in the following analysis, the weight of the SED in the optical will overwhelm the other data. We thus use u^* taken on the CFH telescope; g^+ , r^+ , i^+ , z^+ on the Subaru telescope; and K_s on the CTIO 4-m telescope. Aperture photometry with a 3-arcsec diameter is given in the catalogue. We applied the correction to the total magnitude as described by Capak et al. (2007). The aperture photometry with a 2.9-arcsec diameter given in the

Table 2. Optical and 2- μm photometry of the 10 COSMOS galaxies.

No.	u*	g+	r+	i+	z+	K_s
1	0.530 \pm 0.033	0.924 \pm 0.041	3.04 \pm 0.07	8.43 \pm 0.10	14.2 \pm 0.2	62.6 \pm 3.0
2	0.888 \pm 0.048	1.27 \pm 0.05	3.05 \pm 0.07	7.76 \pm 0.11	13.5 \pm 0.2	63.8 \pm 2.9
3	0.096 \pm 0.022	0.164 \pm 0.024	0.656 \pm 0.034	1.95 \pm 0.06	3.78 \pm 0.11	38.0 \pm 3.0
4	0.892 \pm 0.052	1.50 \pm 0.07	3.97 \pm 0.09	9.52 \pm 0.14	19.2 \pm 0.2	97.8 \pm 4.6
5	2.20 \pm 0.06	2.51 \pm 0.06	5.10 \pm 0.08	9.46 \pm 0.11	13.8 \pm 0.2	44.0 \pm 3.4
6	0.225 \pm 0.023	0.403 \pm 0.003	1.38 \pm 0.05	4.43 \pm 0.08	7.91 \pm 0.13	47.6 \pm 2.9
7	2.07 \pm 0.06	3.22 \pm 0.07	6.50 \pm 0.09	12.6 \pm 0.1	18.4 \pm 0.2	49.3 \pm 3.1
8	1.23 \pm 0.05	1.97 \pm 0.06	4.60 \pm 0.09	11.1 \pm 0.1	18.1 \pm 0.2	75.7 \pm 3.5
9	1.10 \pm 0.04	1.26 \pm 0.04	2.13 \pm 0.06	4.03 \pm 0.07	6.98 \pm 0.12	30.8 \pm 3.1
10	1.13 \pm 0.04	1.83 \pm 0.05	3.68 \pm 0.07	7.73 \pm 0.10	13.8 \pm 0.2	50.6 \pm 3.0

Note. Total fluxes are given in the unit of μJy .

Table 3. *Spitzer* photometry of the 10 COSMOS galaxies.

No.	3.6 μm	4.5 μm	5.8 μm	8.0 μm	24 μm	70 μm
1	106 \pm 0.2	81.6 \pm 0.3	74.7 \pm 1.1	76.5 \pm 2.8	940 \pm 252	20900 \pm 3300
2	89.6 \pm 0.2	73.1 \pm 0.3	66.0 \pm 1.2	58.9 \pm 2.9	797 \pm 19	11700 \pm 2600
3	81.7 \pm 0.2	66.5 \pm 0.3	72.9 \pm 1.2	82.1 \pm 3.0	635 \pm 20	11100 \pm 2600
4	128 \pm 0.7	111 \pm 0.7	78.6 \pm 1.3	87.9 \pm 2.9	780 \pm 22	11600 \pm 2700
5	68.4 \pm 0.2	54.5 \pm 0.3	49.1 \pm 1.2	60.7 \pm 2.8	1000 \pm 92	14200 \pm 2800
6	79.0 \pm 0.2	62.1 \pm 0.3	50.7 \pm 1.2	62.6 \pm 2.7	553 \pm 16	14900 \pm 2700
7	67.2 \pm 0.2	50.1 \pm 0.3	62.5 \pm 1.1	81.4 \pm 2.8	1190 \pm 256	20800 \pm 3100
8	93.0 \pm 0.2	69.8 \pm 0.3	68.9 \pm 1.1	56.4 \pm 2.5	849 \pm 165	9900 \pm 2500
9	57.2 \pm 0.5	51.6 \pm 0.5	35.1 \pm 1.2	53.3 \pm 2.7	573 \pm 179	16100 \pm 2300
10	91.2 \pm 0.2	71.3 \pm 0.3	46.5 \pm 1.1	53.4 \pm 2.9	590 \pm 199	7300 \pm 1800

Note. Total fluxes are given in the unit of μJy .

S-COSMOS IRAC four-channel catalogue was converted to the total fluxes by applying correction factors of 0.90, 0.90, 0.84 and 0.73 for 3.6, 4.5, 5.8 and 8.0 μm , respectively (see README attached to this catalogue). The total fluxes of the COSMOS galaxies are summarized in Tables 2 and 3 in the units of μJy . The SEDs of the 12 galaxies are plotted as a function of the rest wavelength in Fig. 2.

The optical spectra of our 12 galaxies are illustrated in Fig. 3 along with the vertical lines showing the positions of the [O II] λ 3727 emission line from H II regions and the stellar absorption lines, namely, Mg II λ 2798, Ca II H and K, H ζ and H ϵ . [O II] λ 3727 indicates the presence of OB stars, while the absorption lines are useful to measure the age of the relatively old stellar populations (Kawara et al. 2011). The equivalent widths of the lines are given in Table 4 along with the D(Ca II) index. This index is defined as $D(\text{Ca II}) = 2 \times \text{EW}(\text{Ca II K}) / [\text{EW}(\text{H}\zeta) + \text{EW}(\text{Ca II H} + \text{H}\epsilon)]$ (Kawara et al. 2010), where EW(Ca II K), EW(H ζ) and EW(Ca II H + H ϵ) are the equivalent widths of Ca II K, H ζ and the blend of Ca II H and H ϵ , respectively.

Table 5 gives the 8–1000 μm luminosity L_{IR} and the mass of dust M_{d} of the 12 sample galaxies. We obtained L_{IR} by fitting the Dale & Helou (2002) ULIRG template to the 70- μm data except for SST J1604+4304 for which the 70- and 160- μm data were used for fitting. Deriving FIR colours $f_{\nu}(160 \mu\text{m})/f_{\nu}(70 \mu\text{m})$ of 70- μm sources that are not detected at 160 μm from the stacking of the 160- μm data points, Kartaltepe et al. (2010) found that those not detected at 160 μm have hotter FIR colours than those detected at 160 μm , and that the FIR colours of 70- μm sources not detected at 160 μm scatter around the Dale & Helou (2002) ULIRG template at $z \sim 1$. It is thus appropriate to utilize this template to derive L_{IR} for those not detected at 160 μm . The typical uncertainty for L_{IR}

using the 70 μm data is estimated to be ~ 0.2 dex (Kartaltepe et al. 2010). SST J1604+4304 was re-analysed in the same way as the other galaxies. While the Arp 220 template was used to estimate L_{IR} and the dust temperature in our previous analysis (Kawara et al. 2011), we apply the Dale & Helou (2002) ULIRG template in the present analysis. In addition, we include a new term of the dust mass in the minimum χ^2 method. The new results are quite consistent with our previous results.

The dust mass was estimated using the formula of $M_{\text{d}}/f_{\nu} = D_{\text{L}}^2 / [(1+z)\kappa_{\nu_{\text{e}}} B_{\nu_{\text{e}}}(T_{\text{d}})]$, where f_{ν} is the observed flux density at frequency ν , $\nu_{\text{e}} = (1+z)\nu$, D_{L} is the luminosity distance to the emitter, $B_{\nu_{\text{e}}}(T_{\text{d}})$ is the Planck function for T_{d} the temperature of dust at ν_{e} , and $\kappa_{\nu_{\text{e}}}$ is the absorption cross-section per unit dust mass at ν_{e} . As can be seen in this formula, M_{d} depends on the product $\kappa_{\nu} B_{\nu}(T_{\text{d}}) \propto \nu^{\beta} B_{\nu}(T_{\text{d}})$ if $\kappa_{\nu} \propto \nu^{\beta}$.

It is known that there is an anticorrelation between β and T_{d} (Blain, Barnard & Chapman 2003; Bracco et al. 2011). This degeneracy may be due to the intrinsic properties of dust grains or application of a single-temperature model to the SEDs which average various temperatures along the line of sight (Bracco et al. 2011). Thus, when fitting a single-temperature model to the SED, the resultant T_{d} depends on β or the properties of the dust extinction curves; the extinction curves we study here are the MW, pseudo-MW, Calzetti, SN curves, as fully described in Section 3.1.2.

The dust temperatures cannot be directly derived from our data, because of the lack of data longward of 160 μm . We thus estimated T_{d} by fitting to the Dale & Helou (2002) ULIRG template, resulting in $T_{\text{d}} = 40.5 \pm 9.3$ for the SN dust with $\beta \simeq 1.6$ and $T_{\text{d}} = 37.0 \pm 8.9$ for the MW dust with $\beta \simeq 2$; T_{d} derived with the SN dust is 10 per cent higher than that with the MW dust. This temperature difference is expected to result from the degeneracy between β and

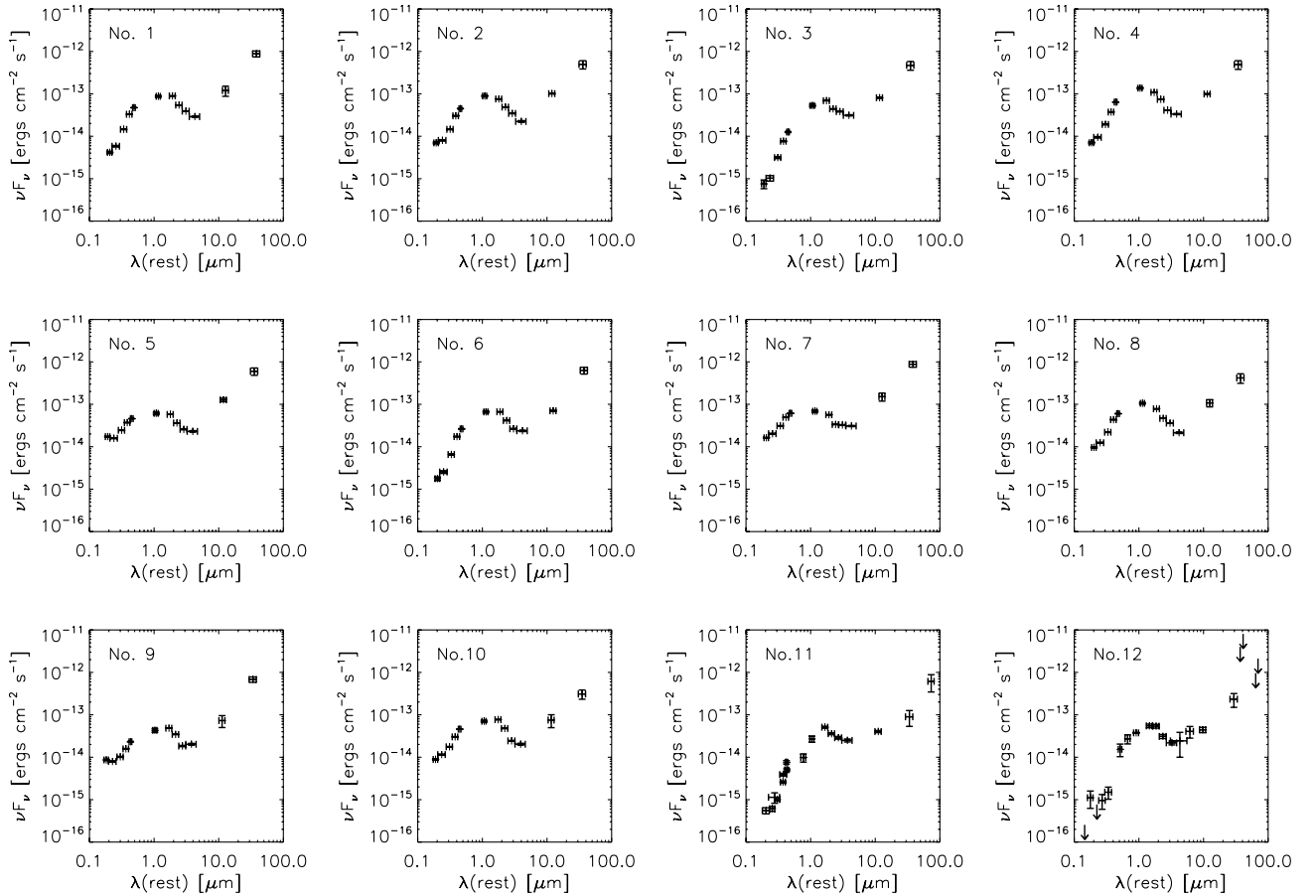


Figure 2. 0.1–100 μm SEDs of the 12 galaxies, illustrating νF_ν ($\text{erg cm}^{-2} \text{s}^{-1}$) as a function of rest wavelength (μm).

T_d . Table 5 gives M_d for the 8–40 M_\odot SN dust. M_d in Table 5 should be multiplied by 0.81 for the 8–30 M_\odot SN dust and 0.78 for the MW dust. It is noted that M_d is derived by using κ_{ν_e} at 80 μm which is $44 \text{ cm}^2 \text{ g}^{-1}$ for MW dust, $24 \text{ cm}^2 \text{ g}^{-1}$ for 8–30 M_\odot SN dust, and $20 \text{ cm}^2 \text{ g}^{-1}$ for 8–40 M_\odot SN dust (see fig. 7 in Kawara et al. 2011).

3 ANALYSIS

We take a similar approach as performed in our previous study. Synthetic spectra of stellar populations reddened by various dust models are applied to reproduce the data of the 12 sample galaxies. For full details of this approach, we refer the reader to Kawara et al. (2011) and references therein.

3.1 Dust

Our dust models are a combination of an optical properties of dust and a geometry of the dust distribution.

3.1.1 Geometries of dust distribution

The attenuation produced by dust in front of an extended source depends not only on the optical properties of dust grains, but also on the geometry of spatial distribution of dust, especially when starlight is attenuated by a thick, clumpy dust layer or dust is internal to the extended source. Analytic solutions to determine the dust parameters for various geometries are extensively studied by Natta

& Panagia (1984) and Code (1973). Code (1973) applied the two-stream approximation to the radiative transfer for a circumstellar dust shell and this approximation was developed for a dust slab containing emitters and absorbers in the appendix by Kawara et al. (2011). It is noted that the slab approach is a good approximation to a spherical geometry. The reader may also refer to an excellent review and discussion in Calzetti, Kinney & Storchi-Bergmann (1994).

We consider the following geometries of dust distribution: (1) Internal dust geometry – absorbers (dust grains) and emitters (stars) are uniformly mixed and distributed; (2) Foreground dust screen geometry – absorbers are physically separated from and located in a screen in front of emitters, where we assume that there are N clumps on average along the line of sight, thus the dust distribution is clumpy (small N) or uniform (very large N); (3) Composite geometry – dust grains distribute both within the system of stars as internal dust and in the screen in front of the system.

The effects of dust also depend on the physical distance between the dust and the stars (Calzetti et al. 1994). If the dust is located physically distant from the stars, the effect of dust is to remove photons from the line of sight through absorption and scattering. Hereafter, we call this distant configuration *no scattering*. On the other hand, if the dust is located close to the stars, the effect is not only to remove photons from the line of sight but also to convey photons back into the line of sight by scattering. We examine this close configuration in two extreme cases, namely, *forward-only scattering* and *isotropic scattering*. In the internal dust geometry where the dust is located close to the stars, we account for the effect of the scattering through the relations $\tau_{\text{eff}} = (1 - \gamma)\tau_{\text{ext}}$

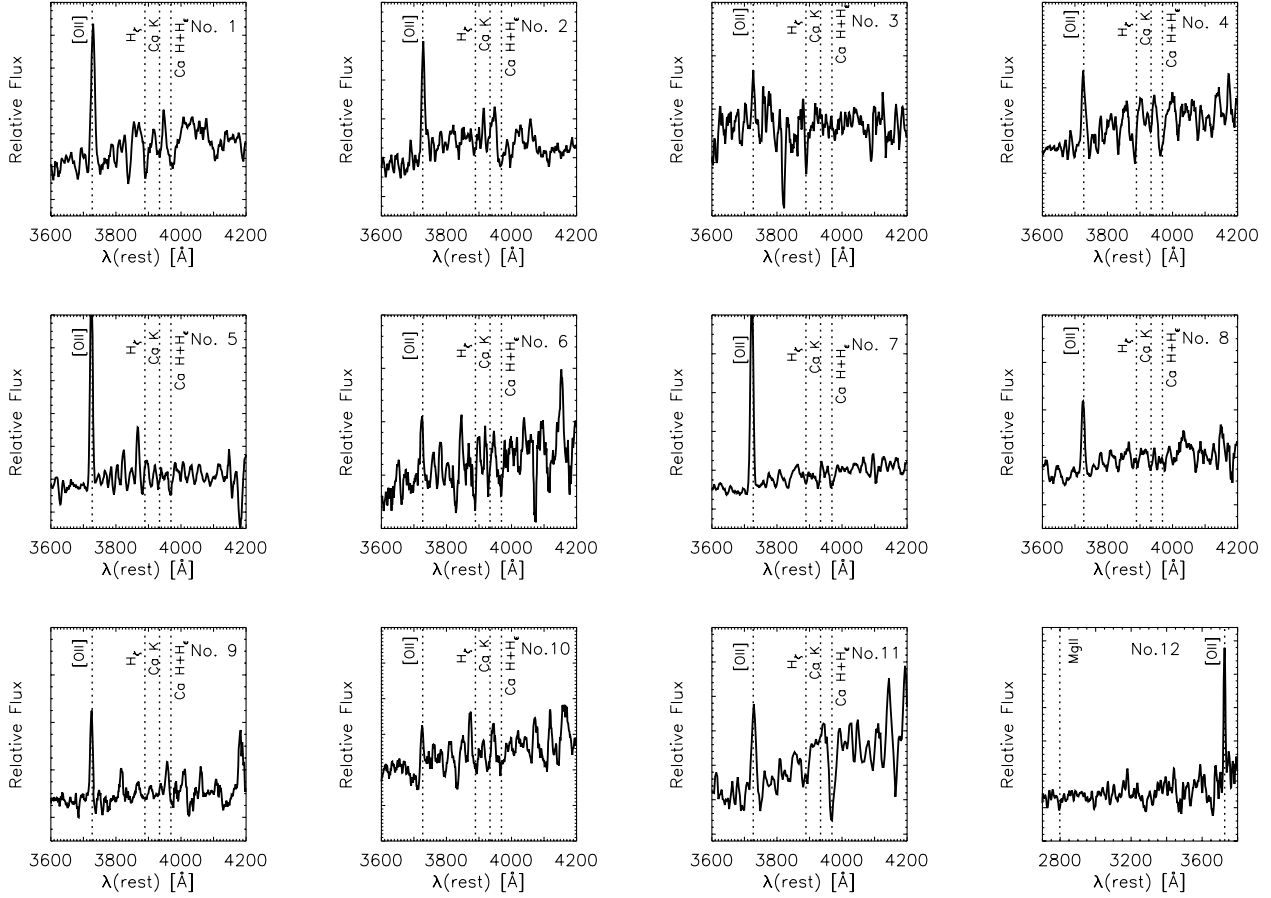


Figure 3. Optical spectra of the 12 galaxies. The relative flux densities (per Å) are plotted as a function of rest-frame wavelength (Å). The vertical lines mark the positions of Mg II at 2798 Å; [O II] at 3727 Å; Ca II H and K at 3968 and 3934 Å, respectively; Hζ at 3889 Å; and Hε at 3970 Å.

Table 4. Spectroscopic properties of the 12 galaxies.

(1) No.	(2) EW([O II]) (Å)	(3) D(Ca II)	(4) EW(Hζ) (Å)	(5) EW(Ca K) (Å)	(6) EW(Ca H + Hε) (Å)
1	45.6 ± 2.4	0.28 ± 0.13	10.6 ± 1.6	3.5 ± 1.5	14.2 ± 2.2
2	27.3 ± 2.7	0.11 ± 0.13	4.3 ± 1.9	1.0 ± 1.1	12.8 ± 1.5
3	10.1 ± 3.5	0.27 ± 0.36	12.6 ± 5.2	2.6 ± 3.4	6.8 ± 3.8
4	31.4 ± 3.3	0.15 ± 0.05	6.5 ± 1.4	1.6 ± 0.6	15.4 ± 1.2
5	65.3 ± 1.8	0.18 ± 0.22	6.4 ± 2.6	1.0 ± 1.2	4.7 ± 1.9
6	9.8 ± 1.8	0.51 ± 0.26	8.4 ± 3.7	4.9 ± 2.2	10.8 ± 2.6
7	35.0 ± 0.6	0.13 ± 0.26	1.8 ± 0.6	0.3 ± 0.6	2.9 ± 0.7
8	23.4 ± 1.3	0.18 ± 0.41	3.6 ± 1.0	0.6 ± 1.2	2.6 ± 2.3
9	63.2 ± 6.0	0.02 ± 0.14	6.1 ± 1.9	0.1 ± 1.0	9.0 ± 1.9
10	9.1 ± 2.1	0.37 ± 0.26	5.8 ± 2.0	2.6 ± 1.8	8.4 ± 2.4
11 ^a	31.1 ± 4.3	0.03 ± 0.11	7.6 ± 2.1	0.4 ± 1.4	16.7 ± 2.2
12 ^b	47 ± 5		EW(Mg II) = 7.6 ± 3.1		

Note. Column 2 for the equivalent width of the [O II] line at 3727 Å. Column 3 for the Ca II index defined as $D(\text{Ca II}) = 2 \times \text{EW}(\text{Ca II K}) / [\text{EW}(\text{H}\zeta) + \text{EW}(\text{Ca II H} + \text{H}\epsilon)]$ (Kawara et al. 2010). Columns 4–5 for the equivalent width for the Hζ line at 3889 Å and the Ca II K line at 3934 Å, respectively. Column 6 for the equivalent width of the blends of the Ca II H and Hε lines at 3968 and 3970 Å, respectively.

^a The equivalent widths were taken from Kawara et al. (2010).

^b EW([O II]) was taken from Dey et al. (1999), and EW(Mg II λ2798) was measured using the spectrum given by Dey et al. (1999).

Table 5. Infrared luminosity, dust mass and dust shell radius of the 12 galaxies.

No.	L_{IR}^a ($10^{12} L_{\odot}$)	M_{d}^b ($10^8 M_{\odot}$)	r^c (arcsec)
1	2.60 ± 1.14	1.66 ± 1.06	0.63
2	2.87 ± 1.25	1.55 ± 1.02	0.74
3	2.66 ± 1.18	1.73 ± 1.15	0.47
4	2.65 ± 1.20	2.15 ± 1.43	0.52
5	3.73 ± 1.63	2.00 ± 1.30	0.80
6	1.63 ± 0.74	1.42 ± 0.91	0.61
7	2.78 ± 1.21	1.65 ± 1.05	0.85
8	1.82 ± 0.81	0.94 ± 0.63	0.61
9	2.93 ± 1.39	3.30 ± 2.11	0.62
10	2.12 ± 0.95	1.16 ± 0.78	0.60
11	1.04 ± 0.50	1.94 ± 0.91	0.48
12	7.05 ± 3.25	3.72 ± 2.69	0.47

^a L_{IR} is the 8–1000 μm bolometric infrared luminosity.

^bThe 8–40 M_{\odot} SN dust is assumed. For the MW dust, a factor of 0.78 should be multiplied.

^c r is the radius of dust shell. It can be approximated as $r \sim \sqrt{r_x r_y}$ which were obtained from *HST* I_{814} images.

for forward-only scattering and $\tau_{\text{eff}} = (1 - \gamma)^{0.75} \tau_{\text{ext}}$ for isotropic scattering (Kawara et al. 2011), where γ is albedo, τ_{eff} is the effective absorption optical depth, and τ_{ext} is the sum of the optical depth of absorption and scattering. In the foreground screen geometry, if the dust screen is physically distant from the stars, no scattering applies. On the other hand, if the dust screen is physically close to the stars, the scattering can put photons into the line of sight. We thus consider three cases for the foreground geometry: $\tau_{\text{eff}} = \tau_{\text{ext}}$ for no scattering, $\tau_{\text{eff}} = (1 - \gamma)\tau_{\text{ext}}$ for forward-only scattering, and $\tau_{\text{eff}} = (1 - \gamma)^{0.5} \tau_{\text{ext}}$ for isotropic scattering. The relation between the observed flux f_{ν} and the unobscured flux f_{ν}^0 is $f_{\nu}/f_{\nu}^0 = (1 - e^{-\tau_{\text{eff}}})/\tau_{\text{eff}}$ for an internal dust geometry and $f_{\nu}/f_{\nu}^0 = e^{-\tau_{\text{ap}}}$ with $\tau_{\text{ap}} = N(1 - e^{-\tau_{\text{ext}}/N})$ for a dust screen geometry with the number of N clumps along the line of sight (Natta & Panagia 1984). It is noted that there is a definite difference between attenuation and extinction curves; we regard attenuation curves as f_{ν}/f_{ν}^0 and extinction curves as τ_{ext} .

3.1.2 Extinction curves

We examine two extinction curves synthesized in the ejecta of SNe II, the empirical extinction curve derived by Calzetti (2001), the MW extinction curve given by Draine (2003), and the pseudo-MW extinction curve.

The MW extinction curve exhibits a pronounced feature at 2175 \AA . This feature is known to be absent in the typical extinction curves of the SMC and some galaxies. To check the effect of the feature on the extinction law in our galaxies, we create the pseudo-MW extinction curve which is made by removing the 2175 \AA feature, namely the extinction bump and albedo dip, from the MW extinction curve.

The Calzetti extinction curve is based on the attenuation law that was derived in a range from 0.12 to 2.2 μm by analysing local starbursts and blue compact dwarf galaxies (Calzetti et al. 1994). Calzetti (2001) expresses this law in a functional form combined with a geometry of a uniform dust screen with no scattering (i.e. $f_{\nu} = e^{-\tau_{\nu}} f_{\nu}^0$). This cannot be used for longer wavelengths, because the extinction curve (τ_{ν}) sharply drops beyond 2.2 μm . The Calzetti extinction curve is almost identical to the MW curve from 0.6 to 1.6 μm . We thus extend the Calzetti curve to longer

wavelengths by adopting the MW extinction curve for wavelengths $\geq 1.6 \mu\text{m}$. Because the Calzetti curve has already been processed by the foreground screen, we consider this geometry only for the Calzetti curve.

Combining the optical constants in the literature with the grain species and size distribution of SN-condensed dust derived by Nozawa et al. (2003), and using the Mie theory, Hirashita et al. (2005) calculated absorption and scattering cross-sections of homogeneous spherical grains with various sizes condensed in mixed and unmixed ejecta. Comparing their models to the extinction curve of SDSS J1048+637 (a BALQSO at $z \sim 6.2$), Hirashita et al. (2005) suggest the mass range of SN progenitors to be $\lesssim 30 M_{\odot}$, whereas the upper mass of SN progenitors is usually assumed to be $40 M_{\odot}$. We thus adopt the two extinction curves of SNe II for the Salpeter (1955) initial mass function (IMF); one has a mass range of progenitors from 8 to $30 M_{\odot}$, and the other from 8 to $40 M_{\odot}$. These were obtained by interpolating or extrapolating the extinction curves that Hirashita et al. (2005) calculated for unmixed SNe II with progenitor masses of 13, 20, 25 and $30 M_{\odot}$. We adopt these in the present study and call the original SN extinction curves in a sense that the subsequent processing of dust destruction is not considered. Recent studies indicate that the original SN extinction curves become flatter through the reverse shock destruction (Bianchi & Schneider 2007; Hirashita et al. 2008), while Hirashita et al. (2010) show the importance of the shattering in a warm ionized medium (WIM) in starburst environments and this effect makes the extinction curves steeper. They suggest that the final extinction curves, after the reverse shock destruction and the shattering, have a slope similar to that of the original curve. The degree of the reverse shock destruction and shattering critically depends on the assumed parameters, especially gas density of the ISM. Considering these uncertainties and the similarity between the original and final extinction curves, we decided to adopt the original SN extinction curves in the present study.

3.2 Star formation history

The evolutionary synthesis codes given by Bruzual & Charlot (2003) are used to generate synthetic spectra of evolutionary stellar population models. We adopt the Salpeter (1955) IMF with the mass cutoffs of 0.1–100 M_{\odot} . The star formation histories are exponentially declining models with the star formation rate (SFR) $\propto t_{\text{SFR}}^{-1} \exp(-t/t_{\text{SFR}})$, where t_{SFR} is the e-folding time-scale and t is the age. The synthetic spectra are generated in the parameter range as shown in Table 6.

The equivalent widths of $[\text{O II}]\lambda 3727$ and $\text{Mg II}\lambda 2798$, and $D(\text{Ca II})$ were calculated from the synthetic spectra. $[\text{O II}]$ is a nebular line and unpredictable directly from the synthetic spectra. We first obtain the $\text{H}\alpha$ luminosity by counting ionizing photons in the

Table 6. Parameters of synthetic template spectra.

Parameter	Range
Z	0.005–2.5 Z_{\odot} at 0.005, 0.02, 0.2, 0.4, 1.0, 2.5 Z_{\odot}
t	1–6300 Myr in a step of 0.2 dex
t_{SFR}	10–10 000 Myr in a step of 0.3 dex
$A_{0.3 \mu\text{m}}$	0–15 mag in a step 0.1 mag
	15–100 mag in a step of 1 mag

Note. Z , t , t_{SFR} and $A_{0.3 \mu\text{m}}$ are the metallicity, age after the onset of the star formation in Myr, e-folding time-scale of the star formation in Myr, and extinction at 0.3 μm in magnitude, respectively.

synthetic spectra. The metallicity scaling of $[\text{O II}]/\text{H}\alpha$ for the ionized parameter $q = 3 \times 10^7 \text{ cm s}^{-1}$ was given by Kewley, Geller & Jansen (2004). We thus adopt their theoretical curves with an additional condition, which is applied to avoid a negative or unrealistic value, of $[\text{O II}]/\text{H}\alpha > 0.1$. Kewley et al. (2004) estimated the uncertainty in the $[\text{O II}]$ intensity to be ~ 30 per cent.

3.3 Minimum χ^2 method

We search for the best set of parameters by using a minimum χ^2 method as defined below:

$$\chi^2 = \chi_{\text{SED}}^2 + W (\chi_{[\text{O II}]}^2 + \chi_{\text{EW(abs)}}^2 + \chi_{L_{\text{IR}}}^2 + \chi_{M_{\text{d}}}^2). \quad (1)$$

The weighting factor W is introduced to balance the weight between the SED data.²

Each term is defined as

$$\chi_{\text{SED}}^2 = \sum^{N_{\text{filters}}} (F_{\text{obs}} - b F_{\text{temp}})^2 / \sigma_{\text{SED}}^2, \quad (2)$$

$$\chi_{[\text{O II}]}^2 = (\text{EW}([\text{O II}]_{\text{obs}}) - \text{EW}([\text{O II}]_{\text{temp}}))^2 / \sigma_{[\text{O II}]}^2, \quad (3)$$

$$\chi_{\text{EW(abs)}}^2 = (\text{EW(abs)}_{\text{obs}} - \text{EW(abs)}_{\text{temp}})^2 / \sigma_{\text{EW(abs)}}^2, \quad (4)$$

$$\chi_{L_{\text{IR}}}^2 = (L_{\text{IR}} - L_{\text{IR temp}})^2 / \sigma_{L_{\text{IR}}}^2, \quad (5)$$

$$\chi_{M_{\text{d}}}^2 = (M_{\text{d}} - M_{\text{d temp}})^2 / \sigma_{M_{\text{d}}}^2. \quad (6)$$

Equation (2) is related to photometric data of the continuum from stellar atmosphere. b is a normalization constant between the template flux density F_{temp} and the observed F_{obs} , and the number of photometric filters N_{filters} from UV to $5.8 \mu\text{m}$. $8.0\text{-}\mu\text{m}$ data are excluded from the SED data, because dust emission may be significant in the $8.0\text{-}\mu\text{m}$ band. In order to avoid too small and non-realistic a photometric error, 5 per cent of the flux is added in the quadratic form to the photometric error σ_{ph} , i.e. $\sigma_{\text{SED}}^2 = \sigma_{\text{ph}} + (0.05 F_{\text{obs}})^2$.

Equation (3) is related to the $[\text{O II}]$ line from H II regions ionized by young OB stars. $\text{EW}([\text{O II}])$ predicted using the Kewley et al. (2004) theoretical curve contains ~ 30 per cent uncertainty, thus $\sigma_{[\text{O II}]}^2 = \sigma_{\text{EW}([\text{O II}]_{\text{obs}})}^2 + (0.3 \text{EW}([\text{O II}]_{\text{temp}}))^2$, where $\sigma_{\text{EW}([\text{O II}]_{\text{obs}})}^2$ is the observed error. Equation (4) measures the absorption lines in stellar atmosphere. EW(abs) is $\text{EW}(\text{Mg II})$ for HR10 and $\text{D}(\text{Ca II})$ for the others and $\sigma_{\text{EW(abs)}}^2$ is the observed error.

Equation (5) compares L_{IR} given in Table 5 with the prediction from the model, i.e. $L_{\text{IR temp}} \propto \int (f_v^0 - f_v) dv$, where f_v^0 and f_v are intrinsic and reddened synthetic spectra. Equation (6) compares M_{d} derived from FIR data with $M_{\text{d temp}}$ the dust mass estimated from the dust extinction (i.e. optical depth) and the assumed dust geometry. $M_{\text{d temp}}$ was derived as follows. We first assume a composite geometry consisting of screen dust and internal dust. Suppose a spherical shell with a radius of r and a thickness of δr , where the internal and screen dust fills inside and in the shell, respectively. Then, assuming $\delta r/r \ll 1$, the mass of the internal dust is $M_{\text{in}} = 4\pi(\tau_{\text{in}}/\kappa_{\text{ext}})r^2/3$, while that of the screen dust is $M_{\text{sc}} = 4\pi(\tau_{\text{sc}}/\kappa_{\text{ext}})r^2$. τ_{in} and τ_{sc} are τ_{ext} for internal dust and screen dust, respectively, and they are

related to r and δr as $\tau_{\text{in}} = \rho_{\text{in}}\kappa_{\text{ext}}r$ and $\tau_{\text{sc}} = \rho_{\text{sc}}\kappa_{\text{ext}}\delta r$, where ρ_{in} and ρ_{sc} are the mass density of the internal and screen dust, respectively. The dust mass is derived directly from τ_{in} , τ_{sc} and r with no need to assume δr , ρ_{in} and ρ_{sc} . r can be approximated as $r \sim \sqrt{r_x r_y}$ which were obtained from *HST* I_{814} images, where r_x and r_y are the semimajor and the semiminor axes, respectively. r is given in Table 5.

4 RESULTS

The results of the minimum χ^2 analysis are illustrated in Fig. 4. The left-hand panels of the first three rows plot χ_v^2 ($=\chi^2/\nu$, where ν is degree of freedom)³ as a function of $\tau_{\text{in}}/(\tau_{\text{in}} + \tau_{\text{sc}})$ for a composite geometry consisting of uniform screen dust and internal dust; $\tau_{\text{in}}/(\tau_{\text{in}} + \tau_{\text{sc}}) = 0$ for the foreground screen geometry, while $\tau_{\text{in}}/(\tau_{\text{in}} + \tau_{\text{sc}}) = 1$ for the internal dust geometry. The scattering properties are assumed to be no scattering, isotropic scattering ($g = 0$), or forward-only scattering ($g = 1$). In case of no scattering, the scattering properties are no scattering for screen dust and forward scattering for internal dust because no scattering cannot be assumed for internal dust. The middle and right-hand panels of the first three rows show χ_v^2 as a function of N , the number of clumps, along the line of sight in the foreground screen geometry and the composite geometry with $\tau_{\text{in}}/(\tau_{\text{in}} + \tau_{\text{sc}}) = 0.4$. Several linestyles are used to specify the extinction curve: solid lines to the $8\text{--}30 M_{\odot}$ SN curve, dash to the $8\text{--}40 M_{\odot}$ SN, dot to the Calzetti, dash-dotted to the MW, and dash-triple dot to the pseudo-MW.

The four panels in the fourth row plot $A_{0.3 \mu\text{m}}$ the extinction ($\tau_{\text{in}} + \tau_{\text{sc}}$) in magnitude at $0.3 \mu\text{m}$, t the age (i.e. the time after the onset of the star formation) in Myr, Z the metallicity in solar units, and t_{SFR} the e-folding time-scale of star formation in Myr as a function of $\tau_{\text{in}}/(\tau_{\text{in}} + \tau_{\text{sc}})$. The left-hand panel in the bottom row plots the best-fitting SED along with the unreddened SED and the right-hand panel the contour map of $\chi_v^2 - \chi_v^2(\text{min})$ where $\chi_v^2(\text{min})$ is the smallest χ_v^2 among all the models.

The trends of the results are as follows.

- (1) The SN dust curves generally have reducing χ_v^2 as $\tau_{\text{in}}/(\tau_{\text{in}} + \tau_{\text{sc}})$ is approaching zero (more dominated by screen dust) and N approaching ∞ (more uniform screen).
- (2) Some galaxies have a small χ_v^2 in a clumpy foreground screen geometry, especially galaxies numbers 5 and 12 have the minimum χ_v^2 at N of 10 and 3, respectively.
- (3) The MW and pseudo-MW curves sometimes have reducing χ_v^2 as a geometry gets more dominated by internal dust at $\tau_{\text{in}}/(\tau_{\text{in}} + \tau_{\text{sc}}) = 0.8\text{--}0.9$.

The data point around rest $4 \mu\text{m}$ in the SED plots is the IRAC $8.0 \mu\text{m}$ data, and shows an excess from the model for most of the galaxies. As discussed in Section 3.3, the data of this band were not used in the analysis, because dust emission may be significant in this band. The SED plots in Fig. 4 indeed suggest dust emission around $4 \mu\text{m}$.

Table 7 compares the smallest χ_v^2 of the respective extinction curves along with the dust geometry, the scattering property, and the total extinction including internal and screen dust. There are two obvious features: (1) the optical depth ($A_{0.3 \mu\text{m}}$) in the geometry

² The number of photometric data points was chosen so that the SED fitting did not outweigh the other data. However, we found at a later stage of the analysis that the weight of the SED still overwhelmed the other data for many galaxies. W was thus introduced to ensure that the χ^2 of the SED has the similar magnitude as that of the other data. As a result, we obtained $W = 1$ for galaxies 2, 4, 6, 12, and $W = 3$ for the others.

³ Degree of freedom is defined as $\nu = N_{\text{filter}} + 4W - 5$, where N_{filter} is the number of photometric data used for χ_{SED}^2 and W the weighting factor. The number of fitted parameters is 5 (i.e. b , t , t_{SFR} , $A_{0.5 \mu\text{m}}$, Z); $N_{\text{filter}} = 9$ for the COSMOS galaxies, 13 for SST J1604, and 10 for HR 10.

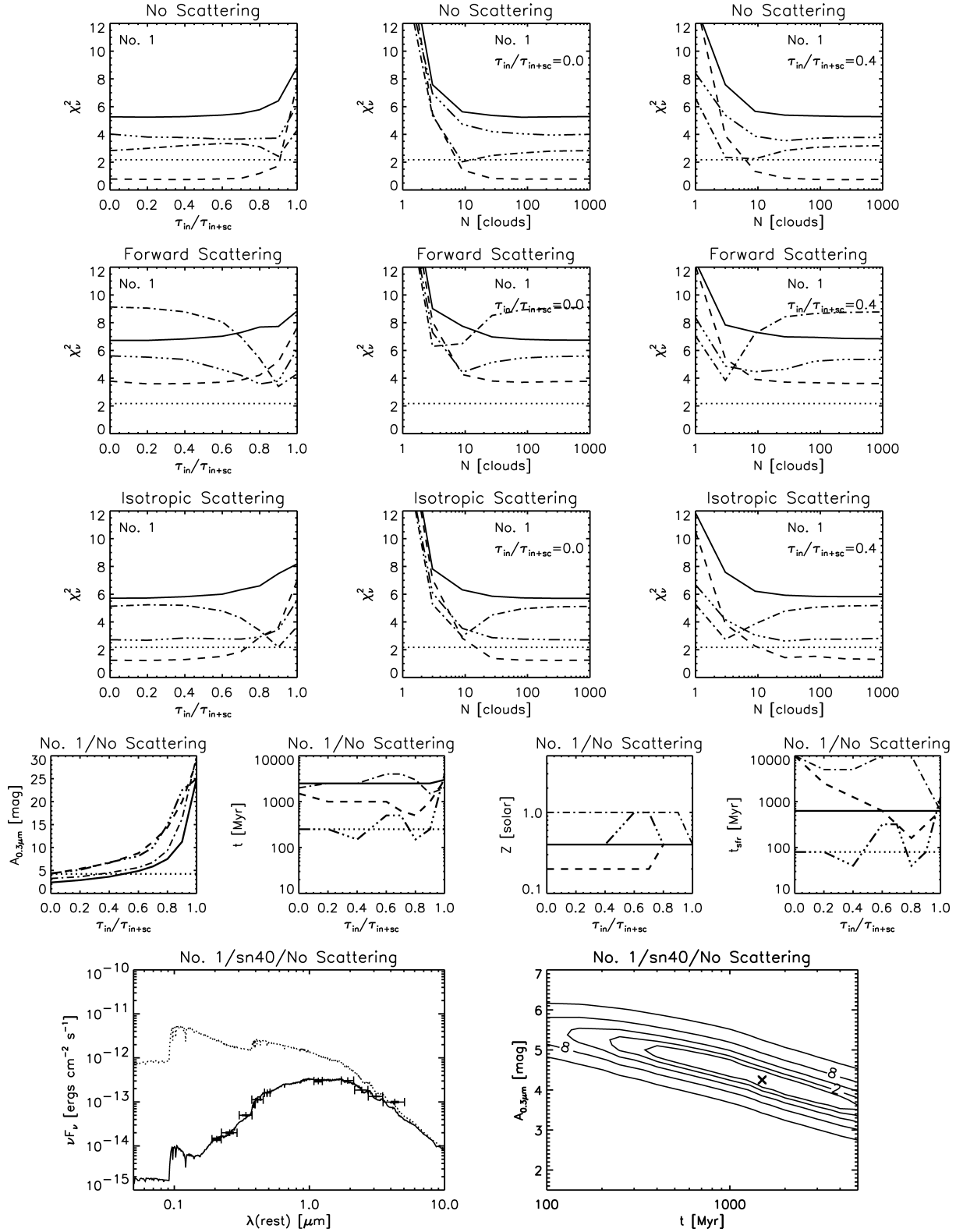


Figure 4. Results of the minimum χ^2 analysis. The source number and the scattering property are indicated in each panel. The left-hand panels in the first three rows show χ_v^2 for a uniform screen as a function of $\tau_{in}/(\tau_{in} + \tau_{sc})$. The middle and right-hand panels in the first three rows represent a screen of N clumps for $\tau_{in}/(\tau_{in} + \tau_{sc}) = 0$ and $\tau_{in}/(\tau_{in} + \tau_{sc}) = 0.4$, respectively. In case of no scattering, the scattering properties are no scattering for screen dust and forward scattering for internal dust. Solid lines represent 8–30 M_\odot SN dust, dashed 8–40 M_\odot SN dust, dash-dot MW dust, and dash-triple dot pseudo-MW dust, dotted the Calzetti dust. The fourth row panels show $\tau_{in} + \tau_{sc}$ at 0.3 μm in magnitude $A_{0.3\mu m}$, the metallicity Z , the age t (yr), and the time-scale t_{SFR} as a function of $\tau_{in}/(\tau_{in} + \tau_{sc})$. The bottom-row panels show the best-fitting SED along with the unreddened SED and the contour map of $\chi_v^2 - \chi_v^2(\min)$. The full version of this figure is available with the online version of the paper – see Supporting Information.

Table 7. Comparison of dust models.

No.	Reduced χ^2 (χ_v^{2a}) $\tau_{\text{in}}/\tau_{\text{in+sc}}$ (N^b)					Scattering property $A_{0.3\mu\text{m}}$				
	MW	pMW	Cal	SN30	SN40	MW	pMW	Cal	SN30	SN40
1	2.18 0.9 (–)	2.72 0.0 (∞)	2.18 –	5.27 0.0 (∞)	0.79* 0.0 (∞)	Isotrop 17.5	Isotrop 7.1	– 4.3	No 2.4	No 4.3
2	3.35 0.9 (–)	2.87 0.6 (–)	2.04 –	3.65 0.0 (∞)	1.61* 0.0 (∞)	Isotrop 14.4	No 7.3	– 3.9	Isotrop 4.1	No 3.4
3	2.09 0.8 (–)	1.98 0.0 (∞)	2.42 –	2.51 0.9 (–)	1.62* 0.0 (∞)	Isotrop 23.8	Isotrop 8.8	– 5.9	No 18.8	No 6.0
4	3.93 0.9 (–)	0.86* 0.0 (∞)	3.02 –	8.72 0.0 (∞)	2.33 0.0 (∞)	Forward 25.0	Isotrop 5.9	– 2.8	No 2.5	No 3.5
5	1.52 0.9 (–)	2.19 0.7 (–)	2.07 –	2.45 0.0 (∞)	0.80* 0.0 (10)	No 13.1	No 7.5	– 3.3	No 2.9	No 4.8
6	1.88 0.8 (–)	1.72 0.0 (∞)	1.61 –	1.51 0.0 (∞)	1.37* 0.0 (∞)	No 11.9	Isotrop 6.8	– 4.3	No 2.8	No 4.9
7	4.30 0.0 (10)	4.59 0.0 (∞)	5.00 –	5.61 0.0 (∞)	2.35* 0.0 (∞)	No 3.3	Isotrop 4.4	– 3.0	No 2.6	No 3.6
8	1.35 0.0 (10)	1.99 0.0 (∞)	1.51 –	3.00 0.0 (∞)	0.98* 0.0 (∞)	No 4.0	Isotrop 5.4	– 3.6	Isotrop 2.9	No 3.6
9	2.15 1.0 (–)	1.02* 0.9 (–)	1.51 –	2.10 0.0 (∞)	1.88 0.0 (10)	No 32.5	Isotrop 21.3	– 3.5	No 3.6	No 4.9
10	2.88 0.8 (–)	1.23 0.0 (∞)	0.75* –	2.37 0.0 (∞)	2.08 0.0 (∞)	Isotrop 9.4	Isotrop 4.5	– 3.6	Foward 4.0	No 3.6
11	5.09 0.0 (10)	5.55 0.9 (–)	5.05 –	3.56* 0.0 (∞)	3.75 0.0 (∞)	No 8.8	Isotrop 42.5	– 5.8	No 5.4	Foward 17.5
12	0.84* 0.4 (3)	0.84* 0.4 (3)	1.36 –	1.71 0.0 (∞)	1.41 0.0 (∞)	Isotrop 20.0	Isotrop 20.0	– 5.0	No 4.0	No 4.4

Note. The smallest χ_v^2 is given per galaxy per dust model. ‘*’ marks χ_v^2 of the best-fitting model for each galaxy. ‘MW’, ‘pMW’, ‘Cal’, ‘SN30’ and ‘SN40’ denote a dust model of the MW, pseudo-MW, Calzetti, 8–30 M_{\odot} SN and 8–40 M_{\odot} SN, respectively. ‘Isotrop’, ‘Forward’ and ‘No’ denote isotropic, forward, and no scattering, respectively.

^a $\chi_v^2 = \chi^2/\nu$, where ν is the degree of freedom.

^b The number of clumps N is given in parentheses for a geometry dominated by foreground screen dust.

dominated by internal dust is several times greater than that in the foreground screen geometry; (2) the MW curve generally has the smallest χ_v^2 in the composite geometry dominated by internal dust, whereas the SN curves do so in the foreground screen geometry, and the pseudo-MW dust model is in midway. Finding a higher optical depth for the internal absorption is an expected and obvious result, because the screen geometry always maximizes the extinction.

The contour plots in Fig. 4 appear to show the age(t)/extinction ($A_{0.3\mu\text{m}}$) degeneracy, suggesting that t and t_{SFR} given in Table 7 are not very accurate. The uncertainties in the age determination were propagated to the uncertainty to determine the stellar mass of galaxies, because the luminosity-to-mass ratio strongly depends on the age of stellar populations. This degeneracy can be resolved by adding data from 100 μm to the submillimetre, greatly reducing the present uncertainty in L_{IR} .

Table 8 summarizes the best-fitting models. Out of our 12 galaxies, 10 (83 per cent) have a pure foreground dust screen, and nine of the 10 galaxies have a uniform foreground screen. Eight (67 per cent) of the 12 galaxies have the best-fitting model with one of the SN dust curves, all of which are associated with a pure foreground dust screen. Internal dust is only significant in two galaxies, both of which have the *best-fitting* models with the MW or pseudo-

MW extinction curve. Because the extinction curves analysed here can be ordered from the steepest to the flattest as the MW, pseudo-MW, Calzetti, 3–40 M_{\odot} SN and 3–30 M_{\odot} SN, the MW and pseudo-MW curves are too steep to agree with a pure foreground screen, and need to be associated with a geometry dominated by internal dust or a clumpy foreground screen to make the attenuation curve flat or grey. This requires a few times more dust mass than that in a pure, uniform foreground screen. Our results indicate that the 8–40 M_{\odot} SN curve with a uniform foreground screen is the best dust model to account for $z \sim 1$ ULIRGs.

5 DISCUSSION

Gordon, Calzetti & Witt (1997) applied models of stars and dust to the SEDs of 30 local starburst galaxies using the MW and SMC extinction curves, and found that the dust has an extinction curve lacking a 2175 Å feature with a slope intermediate between the MW and SMC curves. The dust geometry has a pure foreground screen with clumps. Gaskell et al. (2004) found indications of a very flat extinction curve in the ultraviolet (UV) from an analysis of 1090 AGNs. Large samples of SDSS quasars indicate that the extinction law in quasars at $z < 2.2$ is described by SMC reddening but not by

Table 8. Properties of the best-fitting models.

No. (1)	$\tau_{\text{in}}/\tau_{\text{in+sc}}$ (N) (2)	Dust model (3)	Scattering (4)	χ^2_{ν} (5)	Z (6)	t (7)	t_{SFR} (8)	$A_{0.3\ \mu\text{m}}$ (9)	M_{in} (10)	M_{sc} (11)	M^* (12)	M_{d}/SN (13)
1	0.0 (∞)	SN40	No	0.79	0.2	1500	10000	4.3	–	1.6	27.5	0.0079
2	0.0 (∞)	SN40	No	1.61	1.0	800	630	3.4	–	1.9	6.5	0.031
3	0.0 (∞)	SN40	No	1.62	1.0	60	10	6.0	–	1.0	1.4	0.16
4	0.0 (∞)	pMW	Isotrop	0.86	1.0	100	40	5.9	–	1.3	1.2	0.19
5	0.0 (10)	SN40	No	0.80	0.4	60	20	4.8	–	2.8	1.9	0.25
6	0.0 (∞)	SN40	Isotrop	1.37	1.0	1500	320	4.9	–	1.7	11.3	0.017
7	0.0 (∞)	SN40	No	2.35	0.4	40	10	3.6	–	2.5	0.6	0.38
8	0.0 (∞)	SN40	No	0.98	1.0	150	40	3.6	–	1.2	1.5	0.085
9	0.9 (–)	pMW	Isotrop	1.02	1.0	150	160	21.3	2.4	0.8	1.5	0.23
10	0.0 (∞)	Calzetti	No	0.75	0.4	60	10	3.6	–	1.0	1.0	0.12
11	0.0 (∞)	SN30	No	3.56	1.0	630	160	5.4	–	0.9	3.6	0.058
12	0.4 (3)	MW	Isotrop	0.84	0.4	2000	630	20.0	0.7	2.2	42.0	0.0098
	0.4 (3)	pMW	Isotrop	0.84	0.4	2000	630	20.0	0.7	2.2	42.0	0.0098

Note. Columns 1–5 are defined in Table 7.

Columns 6–9: Metallicity (Z) in solar, age (t) in Myr, e-folding time-scale (t_{SFR}) in Myr, and extinction at $0.3\ \mu\text{m}$ ($A_{0.3\ \mu\text{m}}$) in magnitude, respectively.

Columns 10–11: Mass of internal dust (M_{in}) and screen dust (M_{sc}), respectively, in the unit 10^8 solar mass.

Column 12: Stellar mass (M_*) in the unit $10^{11}\ M_{\odot}$ that is estimated as $L_{\text{IR}}/(L/M_*)$, where L/M_* is the luminosity-to-mass ratio for the stellar population models.

Column 13: Dust mass (M_{d}) per SN where (M_{d}) is in solar units. The number of SNs per galaxy is derived from the IMF of the model of star formation history and integration of all stars with $\gtrsim 8\ M_{\odot}$.

reddening in the LMC and MW (Richards et al. 2003; Hopkins et al. 2004). Gallerani et al. (2010) proposed that reddening of quasars at $z = 3.9$ – 6.4 has a tendency to be flat at $\lambda \lesssim 2000\ \text{\AA}$. Maiolino et al. (2004) found that the BALQSO at $z = 6.2$ requires a flat extinction curve which is quite different from those observed in the MW, LMC and SMC, but in an excellent agreement with the synthetic SN curves (Todini & Ferrara 2001). The flat extinction law that we found in $z \sim 1$ ULIRGs are probably incompatible with the steep SMC-like extinction law reported for $z < 2.2$ AGNs, and in agreement with the flat extinction law found in high-redshift quasars.

It needs to be reiterated that the SN-dust models generally predict flat extinction curves but there are intrinsic differences among the models. Maiolino et al. (2004) adopted the SN-dust model by Todini & Ferrara (2001) to derive the extinction curves expected in high- z quasars. The calculated curves show a flat feature at UV wavelengths as a result of the main contribution of amorphous carbon grains with radii around $300\ \text{\AA}$, added by the minor contributions of small silicate and Fe_3O_4 grains with radii around $20\ \text{\AA}$. Bianchi & Schneider (2007) revisited the dust formation model by Todini & Ferrara (2001) and also followed the evolution of the dust grains from the time of formation to their survival through the passage of the reverse shock. They showed that the reverse shock predominantly destroys small silicate and Fe_3O_4 grains, and the resultant extinction curves become flatter, being dominated by carbon grains whose extinction coefficients are relatively insensitive to wavelengths. On the other hand, Hirashita et al. (2005) calculated the extinction curves using the SN II-dust model by Nozawa et al. (2003). The derived extinction properties more or less depend on the SN progenitor mass, but are quite flat as a result of the dominant contribution of large ($\gtrsim 0.1\ \mu\text{m}$) amorphous carbon or Si grains. As discussed in Section 3.1.2, the reverse shock efficiently destroys small grains (Nozawa et al. 2007), making the extinction curves much flatter than the original curves (see Hirashita et al. 2008).

Then large grains that survive the destruction through the reverse shock are shattered in the WIM, producing a large number of small grains. This finally leads to the extinction curves similar to the original SN extinction curves (Hirashita et al. 2010). The growth of dust grains through accretion in the ISM would also be efficient in infrared galaxies (Dwek 1998; Draine 2009; Michałowski et al. 2010), and also cause flat extinction curves.

As shown in Table 8, our $z \sim 1$ ULIRGs have an age of mostly $t \leq 650$ Myr with four exceptions (i.e. $t = 800, 1500, 1500, 2000$ Myr), a stellar metallicity of $z = 0.2$ – 1.0 solar, and a dust mass of $M_{\text{d}} \sim 10^8\ M_{\odot}$. Michałowski et al. (2010) suggested that AGB stars are not sufficient to form dust at such an early epoch of galaxy evolution history, whereas SN-condensed dust followed by grain growth in the ISM is important to account for the inferred dust mass. It is noted that our analysis cannot rule out a possible contribution from AGB stars, because some observations (Groenewegen 1997; Gauger et al. 1999) suggest that large-sized dust grains are formed in AGB stars and that larger grains have flat extinction curves. The dust mass per SN in our $z \sim 1$ ULIRGs mostly ranges from 0.01 to $0.3\ M_{\odot}$. This should be compared with the theoretical prediction of the dust yield per SN, which is 0.01 – $0.1\ M_{\odot}$ with dust destruction and 0.1 – $1\ M_{\odot}$ per SN without dust destruction. If the ISM process of dust growth is important, the expected yield will be more than these. However, there would be a possible bias effect on the dust mass per SN inferred from the observations, because a significant correlation between the age t and M_{d}/SN can be seen in Table 8. This correlation seems spurious and simply reflects the uncertainty of determining t caused by the t and $A_{0.3\ \mu\text{m}}$ degeneracy, because the mass-to-luminosity ratio strongly depends on t .

Our results indicate that the dust geometry of a pure foreground dust screen generally explains the data of the $z \sim 1$ ULIRGs better than that dominated by internal dust. Colour–colour plots of optical and UV data of local starbursts were compared with various dust distribution models by Gordon et al. (1997), and they found that the

observed spread cannot be explained by the internal dust geometry, but the foreground screen geometry can explain it. Calzetti et al. (1994) also showed that the failure of the internal dust geometry explains the spread of data of local starbursts, suggesting a foreground screen geometry with a flat extinction curve (i.e. Calzetti curve). Meurer et al. (1995) showed that a strong correlation between the FIR excess and the UV spectral slope for local starbursts can be explained by dust in a foreground dust screen geometry with the Calzetti curve, but not by an internal dust geometry. They attributed the dust in a foreground screen to the Galactic winds frequently observed in starbursts that will sweep out any diffuse ISM from the starburst sites on a time-scale of a few Myr (Heckman, Armus & Miley 1990). The foreground dust screen geometry we are looking at in $z \sim 1$ ULIRGs may also result from the dust that was swept by the Galactic winds.

6 CONCLUSIONS

In order to study the extinction law in galaxies (ULIRGs) at $z \sim 1$, we have analysed the multiwavelength photometric and spectroscopic data of 12 ULIRGs which are archived or published in the literature; 10 galaxies come from the COSMOS survey catalogues, and the others are SST J1604+4304 and HR10.

The data are compared with models of stars and dust. We applied five extinction curves, namely the MW, the pseudo-MW which is MW-like without the 2175 Å feature, the Calzetti, and two SN dust curves, by combining with various dust distributions, namely the foreground screen geometry, the internal dust geometry, and the composite geometry with a combination of dust screen and internal dust. Several scattering properties are used: no scattering, isotropic scattering and forward scattering. In case of no scattering, the effect of dust to convey photons into the line of sight is ignored, while this effect is included in isotropic scattering and forward scattering.

The two SN extinction curves that we applied here were calculated by Hirashita et al. (2005) based on the grain properties of SN-condensed dust derived by Nozawa et al. (2003). These SN extinction curves were calculated assuming the unmixed ejecta of SNe II for the Salpeter IMF in a progenitor mass range of 8–30 or 8–40 M_{\odot} and do not include the effects of the reverse shock in the ejecta and interaction between SN dust grains and the ambient ISM.

Employing a minimum χ^2 method, we find that the foreground dust screen geometry, especially combined with the 8–40 M_{\odot} curve, provides a good approximation to the real dust geometry, whereas internal dust is significant only for two galaxies. The SN extinction curves, which are flatter than the other extinction curves, reproduce the data of eight (67 percent) galaxies better than the other curves do. Our $z \sim 1$ ULIRGs require an age of mostly $t \leq 650$ Myr, a stellar metallicity of $z = 0.2$ – 1.0 solar, and a dust mass of $M_d \sim 10^8 M_{\odot}$. Considering these physical features, we conclude that SN-origin dust is the most plausible to account for the vast amount of dust masses and the flat slope of the observed extinction law. The inferred dust mass per SN ranges from 0.01 to 0.4 M_{\odot} .

ACKNOWLEDGMENTS

We thank H. Hirashita for helpful comments and suggestions and Brice Ménard for his critical reading of the final draft. Simon Bianchi provided us with extremely constructive comments and criticism which improved this work very much. This work has been supported in part by Grants-in-Aid for Scientific research (20340038, 22111503) and Specially Promoted Research (20001003) from JPSP.

REFERENCES

- Beelen A., Cox P., Benford D. J., Dowell C. D., Kovács A., Bertoldi F., Omont A., Carilli C. L., 2006, *ApJ*, 642, 694
- Bertoldi F., Carilli C. L., Cox P., Fan X., Strauss M. A., Beelen A., Omont A., Zylka R., 2003, *A&A*, 406, L55
- Bianchi S., Schneider R., 2007, *MNRAS*, 378, 973
- Blain A. W., Barnard V. E., Chapman S. C., 2003, *MNRAS*, 338, 733
- Bracco A. et al., 2011, *MNRAS*, 412, 1151
- Bruzual G., Charlot S., 2003, *MNRAS*, 344, 1000
- Calzetti D., 2001, *PASP*, 113, 1449
- Calzetti D., Kinney A. L., Storchi-Bergmann T., 1994, *ApJ*, 429, 582
- Capak P. et al., 2007, *ApJS*, 172, 99
- Code A. D., 1973, in Greenberg J. M., van de Hulst H. C., eds, *Proc. IAU Symp. 52, Interstellar Dust and Related Topics*. Reidel, Dordrecht, p. 505
- Dale D. A., Helou G., 2002, *ApJ*, 576, 159
- Dey A., Graham J. R., Ivison R. J., Smail I., Wright G. S., Liu M. C., 1999, *ApJ*, 519, 610
- Draine B. T., 2003, *ARA&A*, 41, 241
- Draine B. T., 2009, in Henning T., Grün E., Steinacker J., eds, *ASP Conf. Ser. Vol. 414, Cosmic Dust – Near and Far*. Astron. Soc. Pac., San Francisco, p. 453
- Dwek E., 1998, *ApJ*, 501, 643
- Frazer D. T. et al., 2009, *AJ*, 138, 1261
- Gallerani S. et al., 2010, *A&A*, 523, A85
- Gaskell C. M., Goosmann R. W., Antonucci R. R. J., Whysong D. H., 2004, *ApJ*, 616, 147
- Gauger A., Balega Y. Y., Irrgang P., Osterbart R., Weigelt G., 1999, *A&A*, 346, 505
- Gordon K. D., Calzetti D., Witt A. N., 1997, *ApJ*, 487, 625
- Groenewegen M. A. T., 1997, *A&A*, 317, 503
- Heckman T. M., Armus L., Miley G. K., 1990, *ApJS*, 74, 833
- Hirashita H., Nozawa T., Kozasa T., Ishii T. T., Takeuchi T. T., 2005, *MNRAS*, 357, 1077
- Hirashita H., Nozawa T., Takeuchi T. T., Kozasa T., 2008, *MNRAS*, 384, 1725
- Hirashita H., Nozawa T., Yan H., Kozasa T., 2010, *MNRAS*, 404, 1437
- Hopkins P. F. et al., 2004, *AJ*, 128, 1112
- Kartaltepe J. S. et al., 2010, *ApJ*, 709, 572
- Kawara K. et al., 2010, *MNRAS*, 402, 335
- Kawara K. et al., 2011, *MNRAS*, 412, 1070
- Kewley L. J., Geller M. J., Jansen R. A., 2004, *AJ*, 127, 2002
- Le Floch E. et al., 2009, *ApJ*, 703, 222
- Lilly S. J. et al., 2007, *ApJS*, 172, 70
- Maiolino R., Schneider R., Oliva E., Bianchi S., Ferrara A., Mannucci F., Pedani M., Roca Sogorb M., 2004, *Nat*, 431, 533
- Meurer G. R., Heckman T. M., Leitherer C., Kinney A., Robert C., Garnett D. R., 1995, *AJ*, 110, 2665
- Michałowski M. J., Murphy E. J., Hjorth J., Watson D., Gall C., Dunlop J. S., 2010, *A&A*, 522, A15
- Natta A., Panagia N., 1984, *ApJ*, 287, 228
- Nozawa T., Kozasa T., Umeda H., Maeda K., Nomoto K., 2003, *ApJ*, 598, 785
- Nozawa T., Kozasa T., Habe A., Dwek E., Umeda H., Tominaga N., Maeda K., Nomoto K., 2007, *ApJ*, 666, 955
- Pope A. et al., 2008, *ApJ*, 675, 1171
- Richards G. T. et al., 2003, *AJ*, 126, 1131
- Robson I., Priddey R. S., Isaak K. G., McMahon R. G., 2004, *MNRAS*, 351, L29
- Salpeter E. E., 1955, *ApJ*, 121, 161
- Sanders D. B., Mirabel I. F., 1996, *ARA&A*, 34, 749
- Sanders D. B. et al., 2007, *ApJS*, 172, 86
- Stern D., Chary R. R., Eisenhardt P. R. M., Moustakas L. A., 2006, *AJ*, 132, 1405
- Todini P., Ferrara A., 2001, *MNRAS*, 325, 726
- Trump J. R. et al., 2009, *ApJ*, 696, 1195

Valiante R., Schneider R., Bianchi S., Andersen A. C., 2009, MNRAS, 397, 1661

Valiante R., Schneider R., Salvadori S., Bianchi S., 2011, MNRAS, doi:10.1111/j.1365-2966.2011.19168.x

SUPPORTING INFORMATION

Additional Supporting Information may be found in the online version of this article:

Figure 4. Results of the minimum χ^2 analysis.

Please note: Wiley-Blackwell are not responsible for the content or functionality of any supporting materials supplied by the authors. Any queries (other than missing material) should be directed to the corresponding author for the article.

This paper has been typeset from a $\text{T}_{\text{E}}\text{X}/\text{L}_{\text{A}}\text{T}_{\text{E}}\text{X}$ file prepared by the author.